Metal-insulator transition in (111) SrRuO₃ ultrathin films (EP)

View Online   Export Citation   CrossMark

Ankur Rastogi,[1] (ID) Matthew Brahlek,[1] Jong Mok Ok,[1] Zhaoliang Liao,[1] Changhee Sohn,[1] Samuel Feldman,[2] and Ho Nyung Lee[1,a)] (ID)

AFFILIATIONS

[1] Materials Science and Technology Division, Oak Ridge National Laboratory, Oak Ridge, Tennessee 37831, USA
[2] Department of Physics and Astronomy, University of Tennessee, Knoxville, Tennessee 37916, USA

[a)] Author to whom correspondence should be addressed: hnlee@ornl.gov

ABSTRACT

(111)-oriented transition metal oxide thin films provide a route to developing oxide-based topological quantum materials, but the epitaxial growth is challenging. Here, we present the thickness-dependent electronic and magnetic phase diagrams of coherently strained, phase pure (111)-oriented SrRuO₃ epitaxial films grown on (111) SrTiO₃ substrates using pulsed laser deposition. With decreasing film thickness, it is found that both the metal-to-insulator and magnetic phase transitions occur at the same thickness of 4–5 nm for films grown along both the (111) and the (001) directions. The character of the transport near the metal-insulator transition is, however, distinct for the different directions, which is attributed to the increased electron-electron correlation for (111) SrRuO₃. The findings presented here highlight both the broad challenges as well as the possibilities in modifying correlated materials using dimensional tuning of electronic and magnetic properties.

The ABO_3 perovskites have countless chemical combinations which give rise to diverse electronic and magnetic phases that are critical for both current and future information and energy technologies. Epitaxial synthesis of such perovskites offer routes to manipulate and control these properties by directly modifying the structure, including bond angles and lengths. While this has been predominately utilized over the past few decades to tune the physical properties of (001) orientated perovskites, including ferroic oxides,[1] nickelates,[2,3] and titanates,[4] only a few attempts have been reported so far for perovskites grown along the (111) direction. In going from the (001) orientation to the (111) orientation, the structural motif transitions from cubic to triangular, where the surfaces have buckled honeycomblike lattices, which are prerequisite for realizing many quantum phenomena. For example, this can enable tuning band-structure topology,[5] creating magnetic frustration due to the odd nearest neighbor number that stems from the triangular lattice,[6,7] unconventional superconductivity,[8] and the quantum anomalous Hall state.[9–11] The challenge in realizing (111) orientated systems is synthesizing atomically flat epitaxial films. This is nontrivial since the (111) plane is thermodynamically unstable due to both the highly polar surface and the large bond density per unit area. Since epitaxial growth techniques, such as pulsed laser deposition (PLD), operate in an environment that is often well away from thermodynamic equilibrium, synthesis of (111) oriented epitaxial films is viable.

Here, we report the evolution of the properties of SrRuO₃ films grown on both (111) and (001) SrTiO₃ substrates as the thickness is scaled to the ultrathin regime [herein we refer to (111) and (001) SrRuO₃ films as SRO111 and SRO001, respectively]. SrRuO₃ in the bulk is a ferromagnetic metal with Curie temperature $T_C \approx 160$ K[12,13] and is a Fermi liquid at low temperature (<10 K).[14] When the thickness of SRO001 is scaled down, it has been found that the films remain metallic down to 3 unit cells (UC, 1.58 nm), below which the films transit into an insulating state; simultaneously, the ferromagnetic transition temperature continuously drops below 10 UC (~3.93 nm), and the magnetic moment is sharply reduced below 3 UC.[15] For SRO111, we found that both the critical thickness for the metal-to-insulator transition and the suppression of the magnetic phase occur at the same thickness as SRO001, and the metallic character is consistent for both SRO111 and SRO001. The key difference between SRO111 and SRO001 is the character of the insulating phase close to the metal-insulator transition: SRO111 is found to be driven by variable range hopping (VRH) type conduction dominated

by electron-electron correlation, so-called Efros-Shklovskii (ES) VRH, whereas SRO001 is driven by Mott-type VRH related to the disorder.

SRO111 and SRO001 films were grown by PLD using a KrF excimer laser with a 5 Hz repetition rate and a laser fluence of 2 J/cm^2. To obtain atomically smooth surfaces, SrTiO$_3$ (111) substrates were etched then annealed at 950 $^\circ$C for 3 h [as shown in the supplementary material Fig. S1(a)], and SrTiO$_3$ (001) substrates were similarly prepared by etching in buffered hydrofluoric acid followed by thermal annealing at 1050 $^\circ$C in the air for 90 min to obtain atomically flat TiO$_2$-terminated substrates.[16–19] Following the substrate treatment, SrRuO$_3$ thin films were grown at 750 $^\circ$C under 140 mTorr of oxygen pressure and cooled in 500 Torr of oxygen. XRD 2θ–θ scans are shown in Fig. S2(a) for SRO111 and SRO001. From x-ray reflectivity measurements, the film thickness was determined to be ~45.4 nm for SRO111 and ~47.3 nm for SRO001. To comparatively understand results for SRO111 to SRO001, we use thickness in nanometer rather than UC. Films were grown over a range of thicknesses from ~2.3 nm (10 UC) to ~45.4 nm (200 UC) for SRO111 and ~1.6 nm (4 UC) to ~47.3 nm (120 UC) for SRO001. The occurrences of the 111 and 222 reflections for SRO111 and 001, 002, 003 reflections for SRO001 confirmed that both films were epitaxial. The presence of the Laue oscillations indicates that the films are atomically flat, as shown zoomed-in in Fig. S2(a) for scans about the 222 peak for SRO111 and the 002 peak for SRO001. Further, XRD reciprocal space maps (RSMs) shown in Figs. S2(b) and S2(c) for the thickest SRO001 and SRO111 films, respectively, confirm both films are coherently strained. Magnetotransport measurements were performed using a Quantum Design Physical Property Measurement System (PPMS) using van der Pauw geometry and a Quantum Design Magnetic Property Measurement System (MPMS), respectively.

Evolution of the sheet resistance (R_s) with temperature for SRO111 for different thicknesses is shown in Fig. 1(a). These data indicate that there are three distinct regimes: First, for films thicker than about 5 nm, the films were metallic over the full temperature range as the sheet resistance monotonically decreased with decreasing temperature down to the lowest temperature measured (10 K). In the intermediate regime (2–4 nm), the resistance decreased with decreasing temperature and reached a temperature T_{Rmin}, where there was a minimum in the resistance; below this, the resistance increased with decreasing temperature, which indicated the emergence of an insulating phase. In Fig. 1(a), this is marked by an asterisk (*). For SRO001, the resistance minimum also occurred between 2 and 4 nm (see Fig. S2). The values of T_{Rmin} are plotted in the phase diagram at the end of the paper for both SRO111 and SRO001, where the data show a sharp rise from zero toward room temperature as the films become insulating. Further, the data for SRO111 and SRO001 lay on top of each other. Finally, the data shown in Fig. 1(a) only go down to 2.3 nm. Below this thickness, the films were completely insulating, which marks the third regime. In this regime, the films were too insulating for transport measurements to be performed. The resistivity values of these films are found to be consistent with previous studies.[20,21]

The paramagnetic to ferromagnetic transition appears in the data in Fig. 1(a) as a kink in the resistance vs temperature, which is highlighted by a small arrow. This can be more precisely quantified by plotting the derivative of the resistance vs temperature, as
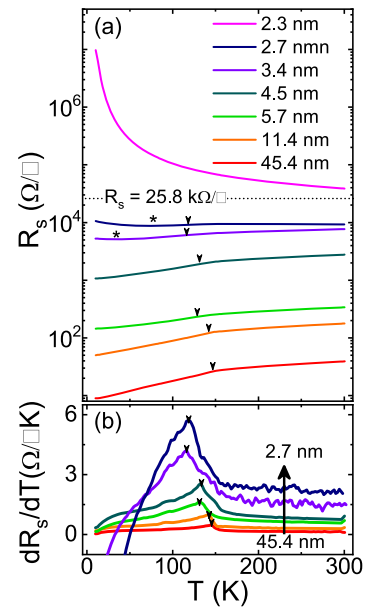

FIG. 1. (a) Temperature-dependent sheet resistance (R_s) for different film thicknesses of SrRuO$_3$ (111) films. The dashed line corresponds to the value of the quantum of resistance (25.8 kΩ/□). (b) First derivative of the R_S for 2.7–45.4 nm thick films. The arrows in both (a) and (b) correspond to the magnetic transition from paramagnetic metallic to ferromagnetic metallic phase as the temperature decreases.

has been done in Fig. 1(b), where the peak marks the transition temperature T_C. These values agree with the transition temperature extracted from magnetization measurements, as shown in Fig. S4 for both SRO111 and SRO001. The extracted values of T_C are compiled in the phase diagram in Fig. 5 as squares, where the data for both SRO111 and SRO001 again overlap. In the thick-limit (>50 nm), T_C approached the bulk value of T_C of 160 K; for thinner samples (10–50 nm), T_C only showed a weak thickness dependence, and below the metal-insulator transition (<4–5 nm), T_C sharply decreased. However, it can further be seen that T_C remains finite as the films become insulating at reduced thickness (~2.3 nm), which indicates that residual magnetism remains in this regime, as has been studied previously.[15] Next, we discuss the scaling of resistance in the metallic regime (>5 nm), then discuss the scaling in the intermediate regime (2–4 nm).

From a temperature dependent sheet resistance of the form $R_S(T) = R_0 + A_n T^n$, where R_0 is the zero-temperature saturation resistance and A_n is the resistance prefactor, the value of the exponent n gives insight into the dominant scattering mechanism. Extraction of n is commonly done by plotting R vs T^n, where n is varied until the data appears linear, but this is often unreliable;[22] instead, plotting the derivative of R_S with respect to T^n (i.e., dR_s/dT^n), where n is varied until the data appears constant is less subjective.[22] This procedure was performed and is shown in Fig. 2(a) and Fig. S5 for SRO111 and in Fig. S6 for SRO001. It was found that for films >5 nm, $n \approx 1.3 \pm 0.1$ over an approximately constant temperature of $T_{min} = 20$ K to $T_{max} = 60$ K (since it is within the estimated experimental error of $\Delta n \approx \pm 0.1$, we take the power to be 4/3).

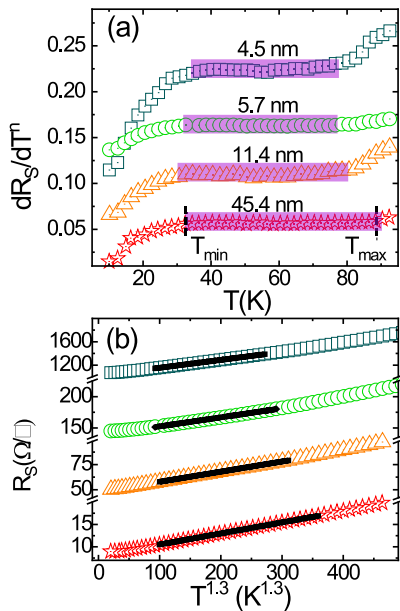**FIG. 2**. (a) Derivative of R_s for SrRuO$_3$ (111) with respect to T^n, dR_s/dT^n, with power index $n \approx 1.3 \pm 0.1$. The thick lines highlight the temperature region over which the derivative is constant. (b) Constant regions found in (a) can be equivalently seen as a linear relation between R_s and $T^{1.3}$.

For consistency, R_S is plotted vs $T^{1.3}$ in Fig. 2(b), where it can be seen clearly that the data are linear over the above-specified range. The scaling power of $n \approx 4/3$, is characteristic of non-Fermi liquids,[23–25] in that, it is not described by simple scattering mechanisms (electron-electron-T^2, electron-phonon-T^1 or-T^{5} [26]). Furthermore, within the framework of self-consistent spin fluctuation theory,[27] a non-Fermi liquid behavior of $R_S \sim T^{4/3}$ is indicative of 2D ferromagnets. For SrRuO$_3$ specifically, Kostic *et al.*[28] also found unusual frequency dependence at 40 K in their infrared spectroscopy measurements, and a similar crossover temperature range from Fermi liquid to non-Fermi liquid was observed by Wang *et al.*[29] where it was argued that local spin fluctuation governed the non-Fermi liquid behavior in SRO001. As shown in Fig. S5 for SRO111 and in Fig. S6(b) for SRO001, for temperatures below this non-Fermi liquid regime, the dominant scattering mechanism transitions to a power consistent with T^2 (fitting yields $n = 1.9 \pm 0.1$) due to electron-electron scattering of a Fermi liquid at low temperature, and finally to a temperature independent regime characteristic of scattering by static disorder at the lowest temperatures. These temperature regimes are summarized in the phase diagram shown in Fig. 5.

The transition from metallic to insulating (between 2 and 4 nm for both SRO111 and SRO001) phases is characterized by several unique insulating phases. This can be revealed by scaling the resistance vs temperature below T_{Rmin}. Interestingly, SRO111 and SRO001 showed different scaling behaviors. For VRH, the conductivity takes the form of $\sigma(T) = \sigma_{0,VRH} \mathrm{Exp}[(T/T_0)^\nu]$, where $\sigma_{0,VRH}$ is the conductivity prefactor, T_0 is the energy scale for hopping conductivity, and the value of ν characterizes the type of hopping.

For the Mott-type VRH, ν takes the form of $1/(d + 1)$, where $d = 2$ or 3 ($\nu = 1/3$ or 1/4, respectively), corresponding to the effective dimensionality of the system.[30] Other exponents do appear that are not consistent with Mott-VRH; for example, ES VRH shows $\nu = 1/2$, which is characteristic of strong electron-electron interactions (i.e., a large Coulomb interaction) with a suppression of the density of states near the Fermi level, which is independent of the effective dimensionality of the transport.[31,32] In Figs. 3(a) and 3(b), we show the conductivity scaled in the form of VRH for 2.3 nm SRO111 and 1.6 nm SRO001, respectively. Varying ν it is found that the data are linear for $\nu \approx 0.48$ ($\sim 1/2$) for SRO111, consistent with ES-VRH, and $\nu \approx 0.35$ ($\sim 1/3$) for SRO001, consistent with 2D Mott VRH.

For thicker samples, it was found that the transport transitions to a weak localization (WL) regime, which requires a finite density of states, consistent with T_{Rmin} being less than room temperature. In the 2D case, the correction to the conductance takes the form $pe^2/(\pi h)\ln(T/T'_0)$, where e is the electron charge, h is Planck's constant, T'_0 is the energy scale related to the transport mean free path and represents the lower length cutoff for diffusive motion, and p is an exponent which is related to the inelastic scattering length by $l_i \propto T^{p/2}$ and reflects the dominant scattering mechanism:[33] $p = 1$ indicates electron-electron (*e-e*) collisions and $p = 3$ indicates electron-phonon (*e-p*). Figure 3(c) shows the variation of sheet conductance G_s plotted vs $\ln(T)$ for 2.7 nm SRO111 and 2.4 nm SRO001, both of which can be seen to be linear. Linear fits yield the slopes of $pe^2/(\pi h) \approx 1.14 \times 10^{-5}$ S for SRO111 and $\sim 4.20 \times 10^{-5}$ S for SRO001; this corresponds to values of p of 1.03 for SRO111 and 3.40 for SRO001. These values indicate that the electron-electron scattering governs the phase relaxation in SRO111 at this thickness,
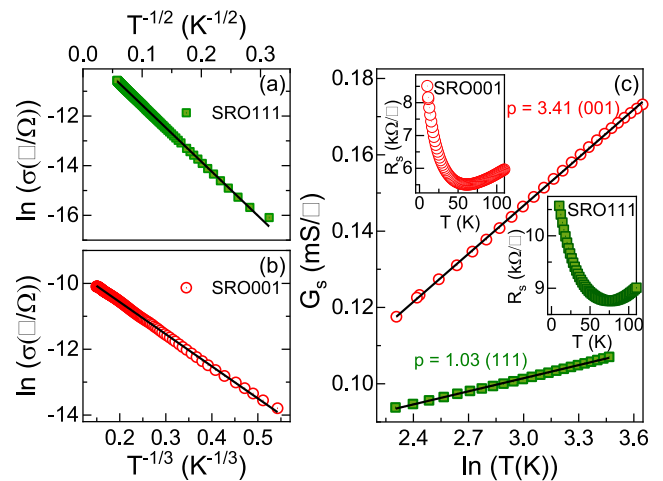

FIG. 3. [(a) and (b)] Logarithmic plots of the conductivity vs $T^{-\nu}$, where $\nu = 1/3$ (2D Mott-VRH) in the case of $\nu = 1/2$ (ES-VRH) for (a) a 2.3 nm thick (111) SrRuO$_3$ film and (b) a 1.6 nm (001) SrRuO$_3$. The solid black lines in panels (a) and (b) are the fits to 2D Mott-VRH and ES-VRH, respectively. (c) Variation of low-temperature conductance with $\ln(T)$ in the intermediate thickness regime where weak localization seems to be a potential cause for an upturn in the resistance. The solid lines are the linear fits and $p \approx 3.41$ for a (001)-oriented 2.4 nm thick SrRuO$_3$ film (circles), while $p \approx 1.03$ for a 2.3 nm thick (111) SrRuO$_3$ film (squares). The insets show the sheet resistance of the two samples on a linear scale.

while electron-phonon scattering dominates SRO001, consistent with previous reports for SRO001.[34]

The temperature dependence of the magnetoresistance is shown in Figs. 4(a) and 4(b) for 2.7 nm SRO111 and 2.4 nm SRO001, respectively, with the field orientated perpendicular in the main panel (in the inset is a comparison of perpendicular and parallel at 10 K). For both SRO111 and SRO001, the magnetoresistance is negative, has a weak butterflylike hysteresis, and has an overall cusplike shape. This cusplike feature is characteristic of WL, which correlated with the upturn in resistance shown in Fig. 1(a) and the inset of Fig. 3(c). Figure 4(c) shows a change in conductance $[\Delta G_s = G_s(H) - G_s(H = 0 \text{ T})]$ vs H, the applied magnetic field, in the units of $e^2/(\pi\hbar)$ as a function of temperature. These data were fitted using $\Delta G_s/\left(\frac{e^2}{\pi\hbar}\right) = \left[\Psi\left(\frac{1}{2} + \frac{H_i}{H}\right) + \ln\left(\frac{H}{H_i}\right)\right]$, Ψ is the digamma function, $H_i = \hbar/(2el_i^2)$ is the characteristic field scale which is related to l_i the inelastic scattering length;[33] the results of the fits are plotted in Fig. 4(c) for SRO111 as solid black curves (data for STO001 are shown in Fig. S7). The temperature dependence of the fitting parameter l_i are plotted in Fig. 4(d). Several things can be noted from this data. First, the scale of l_i is larger for SRO001 in comparison to SRO111; this is indicative of SRO001 being cleaner than SRO111. Second, an approximate power law scaling with temperature can be seen as the data follow a linear trend when plotted in a log-log scale, which agrees with the theoretical prediction of $l_i \propto T^{p/2}$. Using the previous extracted exponents of $p = 1.03$ for SRO111 and $p = 3.41$ for SRO001, we have plotted l_i as solid lines
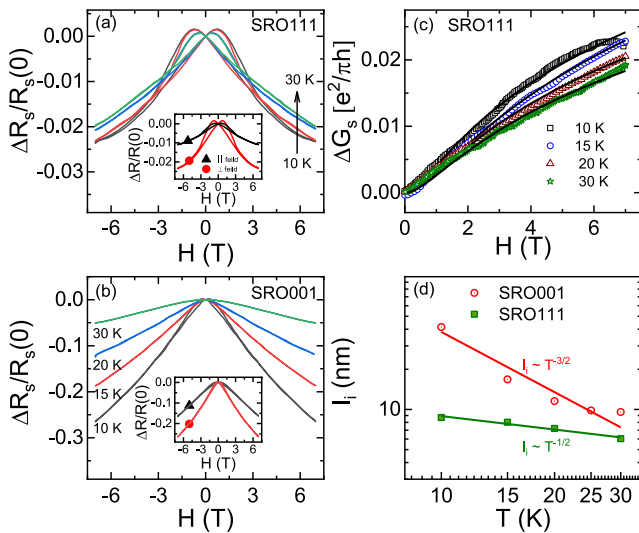
in Fig. 4(d), where it can be seen to agree well with the temperature dependence of l_i for both SRO111 and SRO001, which further confirms the weak antilocalization interpretation.

Finally, we discuss the complete electronic phase diagrams of the SRO111 in comparison to SRO001 thin films shown in Fig. 5. In the thick limit, both SRO111 and SRO001 are metallic ($t > 5$ nm); the resistance vs temperature reveals noninteger scaling characteristic of non-Fermi liquidlike scattering above ~20 K, and below this, a Fermi liquidlike state emerges with resistivity scaling as T^2, as highlighted in Fig. 5 as light blue and pink regions, respectively. The agreement in the observed behavior of both films types in this regime reveals that different crystal growth direction plays only a small role—i.e., any modification of bond angles and length due to epitaxial strain are small enough not to alter the electronic properties or SrRuO$_3$ in this bulklike limit. In going toward thinner films, a resistive upturn is first observed below 5 nm, which coincided with both the resistance per square exactly crossing the resistance quantum of $h/e^2 \approx 25.8$ kΩ/□. This indicates a 2D insulating state and coincides with the initial suppression of ferromagnetism. The weak upturn in resistance below room temperature was characterized by a WL transition at about 3–4 nm and a VRH transition at about 2–3 nm, which are highlighted in Fig. 5 as blue and green regions, respectively. In contrast to the metallic state properties in the thick limit, the characteristics of the VRH and WL are distinct for SRO111 and SRO001. Temperature dependence revealed that the dephasing mechanisms for the WL are primarily electron-phonon for SRO001 and electron-electron for SRO111. The VRH for SRO001 is 2D Mott-type, whereas for SRO111 the VRH is of ES type, indicating enhanced electron-electron correlations in this regime. Disorder likely plays an important role in the transition of both SRO111 and SRO001. Since the resistivity is larger and the inelastic
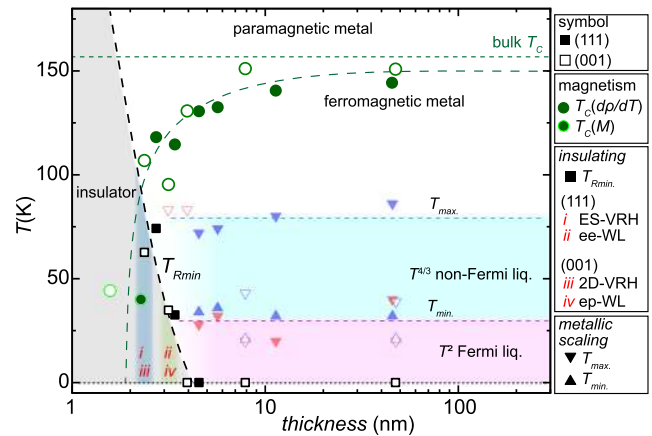

FIG. 4. [(a) and (b)] Magnetoresistance $[\Delta R_S/R_S(0)]$, where $\Delta R_S = R_S(H) - R_S(0)$, at various temperatures for (a) 2.3 nm (111) SrRuO$_3$ film and (b) 2.4 nm thick (001) SrRuO$_3$ film. The applied magnetic field (H) is perpendicular to the film plane. In the insets of (a) and (b), we compare the $\Delta R_S/R_S(0)$ for H applied in-plane and out-of-plane at 10 K. (c) Magnetoconductance (ΔG) in the units of $e^2/(\pi\hbar)$ at different temperatures. The solid black lines are the fits to the weak localization equation as described in the text. (d) Inelastic scattering length (l_i) extracted from the fitting in (c). Solid lines are the theoretical curves $l_i \propto T^{p/2}$ (green, $p = 1$) and $T^{-3/2}$ (red, $p = 3$), where the values of p were taken from the fitting shown in (c).

FIG. 5. Thickness-dependent scaling behavior of electronic and magnetic phases of (111) and (001) SrRuO$_3$ thin films, which are specified as solid and open symbols, respectively. Depending on the thickness of the films, various metallic, insulating, and magnetic phases emerge as specified in the legend on the right. Within the legend T_C is the magnetic transition temperature; Efros-Shklovskii correlation-induced hopping transport and 2D Mott-type variable range hopping are ES-VRH and 2D-VRH, respectively; weak localization due to electron-electron and electron-phonon are ee-WL and ep-WL, respectively; $T_{Max.}$ and $T_{Min.}$ indicate the temperatures at which the resistance is maximum or minimum, respectively.

scattering lengths are lower for SRO111 than SRO001, disorder is higher for SRO111, which highlights the challenge of growing perovskites along the (111) direction. As such, the higher disorder more likely suppresses the density of states for SRO111 and for SRO001, which should reduce the effective screening and thus enhance the Coulomb interaction.

In summary, phase-pure epitaxial $SrRuO_3$ films have been grown on (111) and (001) oriented single-crystal $SrTiO_3$ substrates using pulsed laser deposition. The similarities and differences between the two films have been characterized and summarized in Fig. 5. The physical properties in the thick limit are nominally consistent, while the key differences between SRO111 and SRO001 occur near the metal-insulator transition. In particular, electron-electron scattering appears to be enhanced for SRO111 relative to SRO001. Although the origin still remains unclear, a likely explanation includes the effect of disorder. Confirmation of this requires future investigations. For example, spatially resolved probes of the density of states such as scanning tunneling microscopy would provide crucial information as to the local defect structures in both SRO111 and SRO001 and the relation to the global properties. In closing, the present work highlights opportunities as well as the challenges for perovskite thin films via epitaxy along the (111)-direction.

See the supplementary material for additional data for (111)-oriented $SrRuO_3$ and (001)-oriented $SrRuO_3$.

REFERENCES

[1] D. G. Schlom, L.-Q. Chen, C. J. Fennie, V. Gopalan, D. A. Muller, X. Pan, R. Ramesh, and R. Uecker, MRS Bull. **39**(2), 118 (2014).

[2] J. R. Petrie, V. R. Cooper, J. W. Freeland, T. L. Meyer, Z. Zhang, D. A. Lutterman, and H. N. Lee, J. Am. Chem. Soc. **138**(8), 2488 (2016).

[3] E. J. Moon, B. A. Gray, A. Pimpinelli, M. Kareev, D. Meyers, and J. Chakhalian, Cryst. Growth Des. **13**(6), 2256 (2013).

[4] J. H. Lee, L. Fang, E. Vlahos, X. Ke, Y. W. Jung, L. F. Kourkoutis, J.-W. Kim, P. J. Ryan, T. Heeg, M. Roeckerath, V. Goian, M. Bernhagen, R. Uecker, P. Chris Hammel, K. M. Rabe, S. Kamba, J. Schubert, J. W. Freeland, D. A. Muller, C. J. Fennie, P. Schiffer, V. Gopalan, E. Johnston-Halperin, and D. G. Schlom, Nature **466**, 954 (2010).

[5] S. Okamoto and D. Xiao, J. Phys. Soc. Jpn. **87**(4), 041006 (2018).

[6] S. Nishimoto, V. M. Katukuri, V. Yushankhai, H. Stoll, U. K. Rößler, L. Hozoi, I. Rousochatzakis, and J. van den Brink, Nat. Commun. **7**, 10273 (2016).

[7] V. M. Katukuri, S. Nishimoto, V. Yushankhai, A. Stoyanova, H. Kandpal, S. Choi, R. Coldea, I. Rousochatzakis, L. Hozoi, and J. V. D. Brink, New J. Phys. **16**, 013056 (2014).

[8] J. Chaloupka and G. Khaliullin, Phys. Rev. Lett. **100**(1), 016404 (2008).

[9] L. Si, O. Janson, G. Li, Z. Zhong, Z. Liao, G. Koster, and K. Held, Phys. Rev. Lett. **119**(2), 026402 (2017).

[10] D. Xiao, W. Zhu, Y. Ran, N. Nagaosa, and S. Okamoto, Nat. Commun. **2**, 596 (2011).

[11] Y. Wang, Z. Wang, F. Zhong, and X. Dai, Phys. Rev. B **91**(12), 125139 (2015).

[12] P. B. Allen, H. Berger, O. Chauvet, L. Forro, T. Jarlborg, A. Junod, B. Revaz, and G. Santi, Phys. Rev. B **53**(8), 4393 (1996).

[13] G. Koster, L. Klein, W. Siemons, G. Rijnders, J. S. Dodge, C.-B. Eom, D. H. A. Blank, and M. R. Beasley, Rev. Mod. Phys. **84**(1), 253 (2012).

[14] L. Klein, J. S. Dodge, C. H. Ahn, G. J. Snyder, T. H. Geballe, M. R. Beasley, and A. Kapitulnik, Phys. Rev. Lett. **77**(13), 2774 (1996).

[15] J. Xia, W. Siemons, G. Koster, M. R. Beasley, and A. Kapitulnik, Phys. Rev. B **79**(14), 140407 (2009).

[16] J. Chang, Y. S. Park, and S. K. Kim, Appl. Phys. Lett. **92**(15), 152910 (2008).

[17] J. Chang, Y. S. Park, J. W. Lee, and S. K. Kim, J. Cryst. Growth **311**(14), 3771 (2009).

[18] A. Biswas, P. B. Rossen, C. H. Yang, W. Siemons, M. H. Jung, I. K. Yang, R. Ramesh, and Y. H. Jeong, Appl. Phys. Lett. **98**(5), 051904 (2011).

[19] J. G. Connell, B. J. Isaac, G. B. Ekanayake, D. R. Strachan, and S. S. A. Seo, Appl. Phys. Lett. **101**(25), 251607 (2012).

[20] A. J. Grutter, F. J. Wong, E. Arenholz, A. Vailionis, and Y. Suzuki, Phys. Rev. B **85**(13), 134429 (2012).

[21] B. Lee, O. U. Kwon, R. H. Shin, W. Jo, and C. U. Jung, Nanoscale Res. Lett. **9**(1), 8 (2014).

[22] J. Bass, W. P. Pratt, and P. A. Schroeder, Rev. Mod. Phys. **62**(3), 645 (1990).

[23] C. A. Jackson, J. Y. Zhang, C. R. Freeze, and S. Stemmer, Nat. Commun. **5**, 4258 (2014).

[24] S. Middey, J. Chakhalian, P. Mahadevan, J. W. Freeland, A. J. Millis, and D. D. Sarma, Annu. Rev. Mater. Res. **46**(1), 305 (2016).

[25] J. Liu, M. Kargarian, M. Kareev, B. Gray, P. J. Ryan, A. Cruz, N. Tahir, Y.-D. Chuang, J. Guo, J. M. Rondinelli, J. W. Freeland, G. A. Fiete, and J. Chakhalian, Nat. Commun. **4**, 2714 (2013).

[26] N. W. Ashcroft and N. D. Mermin, *Solid State Physics* (Holt, Rinehart, and Winston, New York, 1976).

[27] S. G. Mishra and P. A. Sreeram, Phys. Rev. B **57**(4), 2188 (1998).

[28] P. Kostic, Y. Okada, N. C. Collins, Z. Schlesinger, J. W. Reiner, L. Klein, A. Kapitulnik, T. H. Geballe, and M. R. Beasley, Phys. Rev. Lett. **81**(12), 2498 (1998).

[29] L. M. Wang, H. E. Horng, and H. C. Yang, Phys. Rev. B **70**(1), 014433 (2004).

[30] N. F. Mott, Philos. Mag. **19**(160), 835 (1969).

[31] J. M. D. Coey, M. Viret, L. Ranno, and K. Ounadjela, Phys. Rev. Lett. **75**(21), 3910 (1995).

[32] B. Shklovskii and A. A. Efros, *Electronic Properties of Doped Semiconductors* (Springer-Verlag, Berlin, 1984).

[33] P. A. Lee and T. V. Ramakrishnan, Rev. Mod. Phys. **57**(2), 287 (1985).

[34] X. Shen, X. Qiu, D. Su, S. Zhou, A. Li, and D. Wu, J. Appl. Phys. **117**(1), 015307 (2015).